IEEE Access
Multidisciplinary | Rapid Review | Open Access Journal

Received 7 July 2023, accepted 14 July 2023, date of publication 19 July 2023, date of current version 26 July 2023.

Digital Object Identifier 10.1109/ACCESS.2023.3296856

RESEARCH ARTICLE

Analytical Model for No-Load Magnetic Field, Can Losses, and Temperature of Permanent Magnet Canned Motor

LIANLIAN GAO, HUI LIU, AND QUN NIU
School of Electrical and Electronic Engineering, Harbin University of Science and Technology, Harbin 150080, China
Corresponding author: Lianlian Gao (gaolianlian2018@163.com)

This work was supported in part by the Innovative Talent Project in Heilongjiang Province under Grant UNPYSCT-2020181.

ABSTRACT The stator and rotor can are added to the permanent magnet canned motor (PMCM) to prevent the stator and rotor core corrosion. The can losses accounts for about 40% of the total losses, therewith the temperature problems can be brought in this kind of motors. Based on this, the accurate analytical calculation method of the magnetic field, can losses, and temperature of PMCM is the key to the rapid design of this kind of motor. The no-load magnetic field is solved by the subdomain method, and the harmonic magnetic density is decomposed by Fourier. Secondly, the calculation formula of can losses is proposed based on the law of electromagnetic induction. The derived calculation formula of can losses can separate the can losses into each harmonic can loss. Then, the results of the analytical solution are added into a new thermal network model (TNM) to predict the temperature distribution of the cans accurately. The new TNM of PMCM can consider the influence of uneven heat dissipation of cans and cooling channels. The key is to re-divide the structure of cans and winding and improves its thermal resistance calculation formula. Finally, the effectiveness of the proposed TNM is verified by comparing it with the results of experiment.

INDEX TERMS PMCM, sub-domain method, can losses, TNM.

NOMENCLATURE

R_1	The outer radius of the rotor.
R_2	The outer radius of PM.
R_3	Stator inner radius.
R_4	The outer radius of a notch.
R_{34}	Radius at the boundary of the two layers of coils.
n_1	Rated speed.
Q_s	Number of stator slots.
p	Number of pole pairs.
μ_0, μ_r	Vacuum permeability and relative permeability of PM.
B_r	Residual flux density of PM.
β	Slot width angle.
J, J_{i1}, J_{i2}	Current destiny in the slot.
M	Magnetization vector.
M_r	Radial components of PM magnetization.
θ_m	Center position angle of N-pole of PM.
α	Pole arc coefficient of the PM.
n	Harmonic order of the permanent magnet sub-domain and the air gap sub-domain.
m	Harmonic order of the slot sub-domain.
$A_{1,n}$, $C_{1,n}$	Integration constant for the subdomain of the permanent magnet.
$A_{2,n} \sim D_{2,n}$	Integration constant for the air gap sub-domain.
$A_{3,i,m(ib_0,it_0)}$	Integration constant of the slot domain.
B_{m1}	Fundamental magnetic density.
B_υ	υ-harmonic magnetic density.
τ	Polar distance.
x	Development direction along the circumference.
l_{ef}	The effective length of the core.
V_{m1}	Relative linear velocity between the cans and the fundamental magnetic field.

The associate editor coordinating the review of this manuscript and approving it for publication was Jinquan Xu.

V_υ	Relative linear velocity between the cans and the υ-harmonic magnetic field.
D	The average diameter of cans.
σ_{T_1}, σ_{T_0}	The conductivity of cans material at temperature T_1 and T_0.
r_{m1}, r_{m2}	Inner radius and outer radius of the cans.
δ_m	Temperature coefficient of cans material.
P_{can}, P_{can1}, $P_{can\upsilon}$	Can losses, can fundamental losses and can harmonic losses.
R_{m1}, R_{xv}	Can fundamental resistance and can harmonic resistance.
A, L, k	Heat transfer area, length, and the thermal conductivity of the material.
r_1, r_2	The inner and outer diameter of cylindrical.
l	Cylindrical elements.
T, G, P	Matrix of node temperatures, thermal conductance, and power sources, respectively.
$\lambda_{ep/cu/air}$	Thermal conductivity of the insulation, copper winding, air.
λ_{EQ}	Equivalent heat dissipation coefficient of winding.
R_{wi}, R_{gi}, R_{tr} R_{fs}, R_{iv}	The thermal resistance of wire insulation, ground insulation, winding, filling strips, and impregnating varnish.
R_{eq}	The equivalent thermal resistance of a winding.
d	The axial length of the winding model.
$W_a \sim W_d$	Length of the copper winding, the copper winding with enameled wire, the whole model including copper winding, enameled wire, and epoxy resin (or air).
α_i	Average heat dissipation coefficient in $i-th$ section($i = A \sim K$).
d_i	i^{th} Length of the section. ($i = A \sim K$).
$R_{ac} \sim R_{kc}$	The average heat dissipation coefficient in sections A to section K.
α_s, α_{ss}	Equivalent convection heat dissipation coefficient of the stator can, the rotor can.
L_b, L_d	The total length of stator can and rotor can.
R_{cold}, R_{hot}	Cold coil resistance, hot coil resistance at the moment of power failure.
T_{cold}	The ambient temperature at which R_{cold} is measured and 234.5 is the constant associated with copper coils and is material dependent.

I. INTRODUCTION

The canned motor pump is a combination of pump and motor usually used in nuclear power, aviation and other fields. The quality of the PMCM determines the quality of the canned pump. The stator can and rotor can are installed on both sides of the air gap to separate the transport medium and the motor [1]. The stator can and rotor can made of corrosion-resistant alloy steel will produce large eddy current losses under the action of air gap rotating magnetic field [2], [3]. The can losses accounts for about 30%∼40% of the total losses, which results in a significant reduction in efficiency [4], [5]. At the same time, due to the existence of can losses, the temperature rise of the PMCM is larger than that of the ordinary motor. In addition, the PMCM because of its special applications and special structure, need to ensure that the working process of the tightness, which further increases the PMCM heat dissipation problem [6]. It is important to research the fast calculation method of the magnetic field, can losses, and temperature field of PMCM.

The sub-domain method(SDM) is to divide the two-dimensional plane of the motor into several regions. Based on Maxwell's electromagnetic field theory, partial differential equations are established on each part, after which the equations are solved according to the magnetic field boundary conditions, and the magnetic field distribution in each part is finally obtained. In [7], a sub-domain model that takes into account the effect of tooth tips has been developed to predict the armature reaction field in a surface mounted permanent magnet machine(SMPM). An alternative sub-domain in the form of a generic solution is created, which is more intuitive in terms of mathematical representation [8]. In [9], a SMPM with unequal-thickness permanent magnets and a quasi-squared dodecagonal rotor structure is used as an example. The unequal-thickness permanent magnets are divided symmetrically, and the magnetic fields generated by each pair of divided permanent magnets are superimposed to finally obtain the magnetic field distribution of the motor, which verifies the accuracy of the method. In [10], a combination of sub-domain and magnet equivalent circuit methods are used to predict the cogging torque of SMPM with rotor eccentricity and magnet defects. In [11], the SDM and the angle-preserving transformation method are combined to develop an analytical model of an eccentric slotless permanent magnet motor under no load and rated load, while the stator part of the motor is equated to the surface current distribution in the calculation process, and the final performance parameters such as the magnetic field distribution and the inverse potential torque of the motor are obtained. The SDM has a basic assumption that the rotor and stator core permeability is infinite. Therefore, it will produce large errors when the motor has a large non-linear effect. In [12], the SDM is combined with the magnetic circuit method to consider the magnetic saturation of the stator core. The results are more accurate than the conventional SDM. In [13] and [14] an

analytical method for calculating and optimizing magnetic fields is proposed for pole eccentric surface-mounted and spoke-type permanent magnet motors. The optimal results show the harmonic content of flux density can be reduced a lot by optimizing eccentric distance of eccentric pole arc while fundamental content will reduce a little. In [15], [16], and [17], the design and electromagnetic characteristics of coaxial magnetic gears, permanent magnet brushless motors and vernier permanent magnet motors are respectively analyzed. New design approaches to the motor structure are proposed, all of which improve the performance of the motor.

The thermal network method takes each component of the motor as a heat source, and the voltage of each node of the network is the central average temperature of each component of the engine. By using heat transfer and Kirchhoff's law, the temperature field calculation is transformed into a centralized parameter thermal circuit calculation. Generally, according to the mechanical structure, the TNM is established by rapid analysis using a simplified thermal path model [18]. In [19], the stator temperature distribution is analyzed by finite element software and extended by TNM, so TNM is used as an auxiliary tool for FEA. In addition, the TNM is only applicable to obtain the average temperature of the main components, not to obtain the characteristics such as maximum value and distribution [20]. To solve these shortcomings, equivalent TNM with network structure [21], [22], [23], [24], [25] are proposed. Similar to FEA's mesh method, the ETN method subdivides main components into multiple elements, such as T-shaped element [22], π shaped elements [23], or multi-segment elements [24]. Then, the heat flow cycle equation is established, and the node temperature is obtained to generate an accurate heat distribution [25]. However, the generation of these networks is structure-dependent and limited by many formulas. In reference [26], the thermal conductivity in each unit is constructed by dividing the target area, which undoubtedly increases the modeling difficulty and calculation cost. In addition, when there is a large temperature gradient in the slot, the average winding temperature is inaccurate [27]. Therefore, a practical element modeling method is needed to reduce the modeling and calculation cost, and the essential winding model and cans model are critical to improve the accuracy.

To precisely establish the winding thermal model, several methods are proposed in [28], [29], [30], [31], and [32]. In [28], an equivalent thermal circuit for toroidal winding is proposed and verified. However, the winding temperature is approximately gradientless. Usually, the temperature gradient difference is unavailable in the TN model but unignorable because of the heterogeneous winding composition [29]. To enhance the accuracy, commercial software is employed for over temperature predictions, which is popular at faulty operation. In [30], the thermal model under inter-turn short-circuit conditions is analyzed by FEA for maximum temperature prediction. In [31], fractional-slot concentrated-winding machines are proved to exhibit different temperature and fluid distributions from integer slot distribution winding using the computational fluid dynamics (CFD) software. The FEA and CFD have become the primary methods when high accuracy and local details are required. However, their employments suffer from time-consuming solving processes and cumbersome modeling operations [32].

In this paper, the magnetic field, can losses, and temperature of PMCM are calculated by analytical calculation method. The can part consider the effect caused by the uneven heat dissipation of the cooling channel. Combined with the SDM, the can losses of PMCM is studied as a heat source, and the results of the experiment and analytical method are compared to verify the proposed TNM.

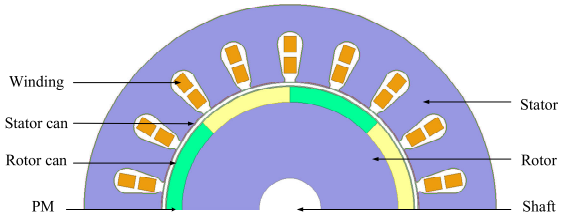

FIGURE 1. A half of the calculation model.

TABLE 1. Parameters of the studied motor.

Quantity	value	Quantity	value
$R_1(\mathrm{mm})$	21	$l_{ef}(\mathrm{mm})$	50
$R_2(\mathrm{mm})$	24	Q_s	18
$R_3(\mathrm{mm})$	25	$\beta(^\circ)$	4.5
$R_4(\mathrm{mm})$	34.68	p	4
$P(\mathrm{kW})$	0.75	$B_r(\mathrm{T})$	1.09
$n_1(\mathrm{r/min})$	3000	α	1

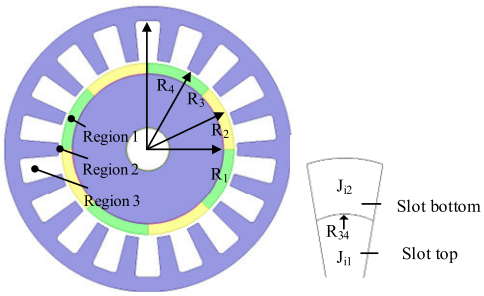

FIGURE 2. Sub-domain model after slot shape equivalence.

II. ANALYTICAL MODEL AND CALCULATION METHOD

A. PMCM STRUCTURE

The main feature of PMCM is the two corrosion-resistant cans respectively placed on each side of the air gap. A 750W

PMCM is taken as an example in this paper. Half of the calculation model is shown in Fig.1. The structure parameters are shown in Table 1. Permanent magnet and cans thicknesses are 3mm and 0.2mm respectively.

B. SDM AND MAGNETIC FIELD CALCULATION

The sub-domain model of the motor discussed in this paper is shown in Fig. 2.

To simplify the calculation, the semi-closed slot is equated to an open slot in building the sub-domain model.The finite element analysis revealed that the presence or absence of the cans has little effect on the air gap magnetic field. However, when solving the air gap magnetic field distribution using the SDM, the permanent magnet sub-domain and the two cans sub-domain equations need to take into account the corresponding eddy currents when considering the effect of the stator and rotor cans, to establish the diffusion equation. The solution to these equations requires the solution of complex Bessel functions. From an analytical point of view, this is doubly difficult. It is therefore ignored. So the can material can be treated as an air gap in the solution. The three sub-domains are divided, with the permanent magnet as the sub-domain 1 region, the air gap as the sub-domain 2 region, and the slot as the sub-domain 3 region. For ease of analysis, the following assumptions are made:

1. The magnetic permeability of the stator and rotor cores is infinite.
2. The relative permeability of the permanent magnets is taken as its actual value.
3. The end effects of the motor are ignored.
4. The stator slots and permanent magnets are of a regular radial sector shape. The stator slot is simplified from a pear-shaped slot to a radially open slot according to the area principle [10].

Using the center of the motor circle as the origin, a two-dimensional polar coordinate system is established on the stator. The partial differential equation satisfied by the vector magnetic potential A in each sub-domain is derived from Maxwell's equations:

$$\nabla^2 \vec{A} = -\mu_0 \mu_r \vec{J} - \mu_0 (\nabla \times \vec{M}) \tag{1}$$

In a two-dimensional magnetic field, since B has only radial and tangential components, the magnetic vector potential has only z-directional components:

$$\begin{cases} \vec{A_1} = A_1(r,\theta) \cdot \vec{e_z} \\ \vec{A_2} = A_2(r,\theta) \cdot \vec{e_z} \\ \vec{A_{3i}} = A_{3i}(r,\theta) \cdot \vec{e_z} \end{cases} \tag{2}$$

To simplify the calculation, two functions are introduced [8]:

$$P_z(x,y) = (\frac{x}{y})^z + (\frac{y}{x})^z \tag{3}$$

$$Q_z(x,y) = (\frac{x}{y})^z - (\frac{y}{x})^z \tag{4}$$

The magnetic vector potential of the permanent magnet subdomain satisfies Poisson's equation:

$$\begin{cases} \dfrac{\partial^2 A_1}{\partial r^2} + \dfrac{1}{r}\dfrac{\partial A_1}{\partial r} + \dfrac{1}{r^2}\dfrac{\partial^2 A_1}{\partial \theta^2} = \dfrac{\mu_0}{r}\dfrac{\partial M_r}{\partial \theta} \\ R_1 \le r \le R_2, \quad 0 \le \theta \le 2\pi \end{cases} \tag{5}$$

At $r = R_1$, the boundary condition can be expressed as:

$$\frac{\partial A_1}{\partial r}\Big|_{r=R_1} = 0 \tag{6}$$

The general solution of the magnetic vector potential of the subdomain of the permanent magnet is obtained by solving according to the separation of variables method:

$$A_1(r,\theta) = \sum_{n=1}^{\infty} A_{1,n} \frac{P_n(r,R_1)}{P_n(R_2,R_1)} \cos(n\theta) + \sum_{n=1}^{\infty} C_{1,n} \frac{P_n(r,R_1)}{P_n(R_2,R_1)} \sin(n\theta) + \eta(r,\theta) \tag{7}$$

The $\eta(r,\theta)$ is the special solution of (5). It can be expressed as:

$$\eta(r,\theta) = \sum_{n=1}^{\infty} X_n(r) \sin[n(\theta_m - \theta)] \tag{8}$$

The $X_n(r)$ can be expressed as:

$$X_n(r) = [\frac{R_1}{n}\left(\frac{R_1}{r}\right)^n f_n'(R_1) + f_n(r)] - \frac{P_n(r,R_1)}{P_n(R_2,R_1)}[\frac{R_1}{n}\left(\frac{R_1}{R_2}\right)^n f_n'(R_1) + f_n(R_2)] \tag{9}$$

$$f_n(r) = \begin{cases} \dfrac{4B_r p}{\pi(1-n^2)} \cdot r \cdot \sin(\dfrac{n\pi}{2p}\alpha), & n/p = 1,3,5\ldots \\ -\dfrac{2pB_r}{n\pi} \cdot r \ln r \cdot \sin(\dfrac{n\pi}{2p}\alpha), & n = p = 1 \\ 0, & else \end{cases} \tag{10}$$

The vector magnetic potentials in the air-gap subdomain satisfy the Laplace equation:

$$\begin{cases} \dfrac{\partial^2 A_2}{\partial r^2} + \dfrac{1}{r}\dfrac{\partial A_2}{\partial r} + \dfrac{1}{r^2}\dfrac{\partial^2 A_2}{\partial \theta^2} = 0 \\ R_2 \le r \le R_3, \quad 0 \le \theta \le 2\pi \end{cases} \tag{11}$$

The solution to the air gap subdomain equation is:

$$A_2(r,\theta) = \sum_{n=1}^{\infty}\left[A_{\mathrm{II},n}\frac{R_2}{n}\frac{P_n(r,R_3)}{Q_n(R_2,R_3)} + B_{\mathrm{II},n}\frac{R_3}{n}\frac{P_n(r,R_2)}{Q_n(R_3,R_2)}\right]\cos(n\theta) + \sum_{n=1}^{\infty}\left[C_{\mathrm{II},n}\frac{R_2}{n}\frac{P_n(r,R_3)}{Q_n(R_2,R_3)} + D_{\mathrm{II},n}\frac{R_3}{n}\frac{P_n(r,R_2)}{Q_n(R_3,R_2)}\right]\sin(n\theta) \tag{12}$$

For the double-layer winding form, the slot area is divided into the top and bottom of the slot. To make the area of the

top of the slot area equal to the area of the bottom of the slot, so that:

$$R_{34} = \sqrt{(R_3^2 + R_4^2)/2} \tag{13}$$

Denoting the magnetic vector potential of the upper, and lower edges of slot i by A_{3it} and A_{3ib}, respectively, the Poisson equation is:

$$\begin{cases} \dfrac{\partial^2 A_{3it}}{\partial r^2} + \dfrac{1}{r}\dfrac{\partial A_{3it}}{\partial r} + \dfrac{1}{r^2}\dfrac{\partial^2 A_{3it}}{\partial \theta^2} = -\mu_0 J_{i1} \\ R_{34} \le r \le R_4, \quad \theta_i \le \theta \le \theta_i + \beta \\ \dfrac{\partial^2 A_{3ib}}{\partial r^2} + \dfrac{1}{r}\dfrac{\partial A_{3ib}}{\partial r} + \dfrac{1}{r^2}\dfrac{\partial^2 A_{3ib}}{\partial \theta^2} = -\mu_0 J_{i2} \\ R_3 \le r \le R_{34}, \quad \theta_i \le \theta \le \theta_i + \beta \end{cases} \tag{14}$$

The boundary conditions for the slotted subdomain are:

$$\begin{cases} \dfrac{\partial A_{3it}}{\partial \theta}\Big|_{\theta=\theta_i} = 0, \dfrac{\partial A_{3ib}}{\partial \theta}\Big|_{\theta=\theta_i} = 0 \\ \dfrac{\partial A_{3it}}{\partial \theta}\Big|_{\theta=\theta_i+\beta} = 0, \dfrac{\partial A_{3ib}}{\partial \theta}\Big|_{\theta=\theta_i+\beta} = 0 \\ \dfrac{\partial A_{3ib}}{\partial r}\Big|_{r=R_4} = 0 \end{cases} \tag{15}$$

The solution for the top region of the slot is:

$$\begin{aligned} A_{3it}(r,\theta) = &\sum_{m=1}^{\infty} A_{\mathrm{III},i,m} \frac{P_{m\pi/\beta}(r,R_4)}{Q_{m\pi/\beta}(R_3,R_4)} \cdot \cos\left[\frac{m\pi}{\beta}(\theta-\theta_i)\right] \\ &+ A_{\mathrm{III},it,0} + \frac{1}{2}\mu_0 J_{i1}(R_{34}^2 \ln r - \frac{1}{2}r^2) \\ &+ \frac{1}{2}\mu_0 J_{i2}(R_4^2 - R_{34}^2)\ln r \end{aligned} \tag{16}$$

The solution for the bottom region of the slot is:

$$\begin{aligned} A_{3ib}(r,\theta) = &\sum_{m=1}^{\infty} A_{\mathrm{III},i,m} \frac{P_{m\pi/\beta}(r,R_4)}{Q_{m\pi/\beta}(R_3,R_4)} \cdot \cos\left[\frac{m\pi}{\beta}(\theta-\theta_i)\right] \\ &+ A_{\mathrm{III},ib,0} + \frac{1}{2}\mu_0 J_{i2}(R_4^2 \ln r - \frac{1}{2}r^2) \end{aligned} \tag{17}$$

The partial differential equations satisfied by each sub-domain are derived from the sub-domain model and given as general solutions. The integration constants in the general solutions need to be solved in conjunction with the boundary conditions.

The boundary conditions at the interface of subdomain 1 and subdomain 2 are:

$$\begin{cases} A_1(R_2,\theta) = A_2(R_2,\theta), & 0 \le \theta \le 2\pi \\ \dfrac{\partial A_1}{\partial r}\Big|_{r=R_2} = \dfrac{\partial A_2}{\partial r}\Big|_{r=R_2}, & 0 \le \theta \le 2\pi \end{cases} \tag{18}$$

The boundary conditions at the interface of subdomain 2 and subdomain 3 are:

$$\begin{cases} A_{3it}(R_{34},\theta) = A_{3ib}(R_{34},\theta) \\ A_{3ib}(R_3,\theta) = A_2(R_3,\theta) \\ \dfrac{\partial A_2}{\partial r}\Big|_{r=R_3} = \dfrac{\partial A_{3ib}}{\partial r}\Big|_{r=R_3} \\ \dfrac{\partial A_{3it}}{\partial r}\Big|_{r=R_{34}} = \dfrac{\partial A_{3ib}}{\partial r}\Big|_{r=R_{34}} \end{cases} \tag{19}$$

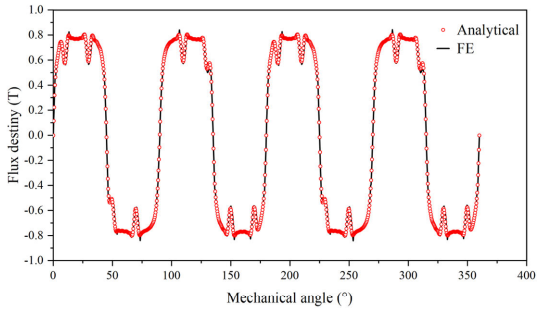

(a)

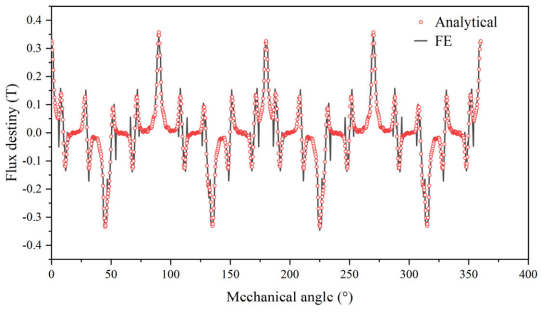

(b)

FIGURE 3. Air gap magnetic density(r = 24.5mm): (a) Radial component. (b) Tangential component.

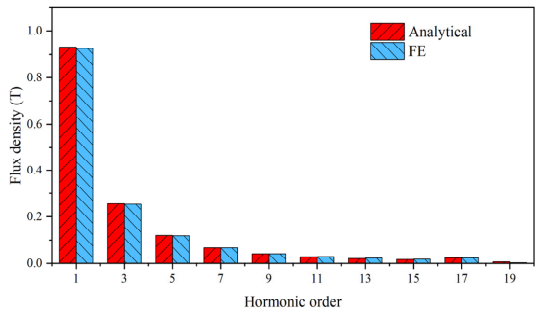

(a)

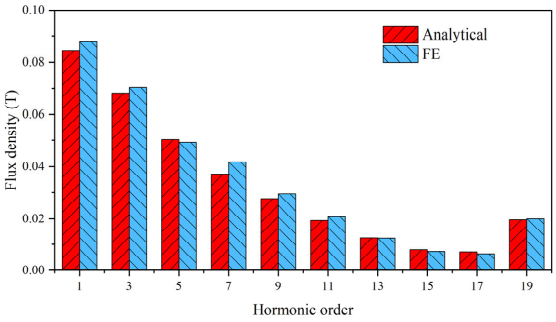

(b)

FIGURE 4. Harmonic decomposition of air gap magnetic: (a) Radial component;(b) Tangential component.

The $A_{\mathrm{I},n}$, $C_{\mathrm{I},n}$, $A_{\mathrm{II},n}$, $B_{\mathrm{II},n}$, $C_{\mathrm{II},n}$, $D_{\mathrm{II},n}$, A_{3it}, A_{3ib} can be determined from the general solution of the equation in each sub-domain and the boundary conditions.

TABLE 2. Efficiency comparison.

Loss type	PMCM	OPM
Stator core losses(W)	9.84	9.71
Rotor core losses(W)	5.41×10^{-3}	5.56×10^{-3}
Stator copper losses(W)	49.79×10^{-3}	49.05×10^{-3}
Rotor can losses(W)	0.236	-
Stator can losses(W)	47.82	-
Eddy current losses in PM(W)	0.457	0.476
Output torque(N · m)	2.22	2.27
Efficiency(%)	86.58	92.33

Based on the relationship between magnetic flux density and magnetic vector position, the expressions for the radial and tangential magnetic densities in the air gap subdomain in polar coordinates can be obtained.

$$B_r = \frac{1}{r}\frac{\partial A_2}{\partial \theta} \tag{20}$$

$$B_\theta = -\frac{\partial A_2}{\partial r} \tag{21}$$

The calculation result of magnetic field distribution is shown in Fig.3. Fig.4 shows the harmonic decomposition graphs in two cases. The harmonic components in the two cases are also very consistent. As the polar arc factor of the motor model in this paper is 1, the greater the polar arc factor, the higher the air gap magnetic density and therefore the slightly higher the amplitude of each harmonic at equal air gap lengths.

C. LOSS CALCULATION

The can is made of metal alloy. The stator and rotor cores of the PMCM are made of silicon steel sheets. As an integral part, the cans cannot effectively suppress eddy currents like the stator and rotor cores laminated structure. Small changes in magnetic flux can lead to large eddy current losses.

The losses of ordinary permanent magnet motors include stator copper losses, stator core losses, etc. The stator can and rotor can are added to the PMCM. The losses in PMCM include stator copper losses, stator core losses, stator can losses and rotor can losses. The efficiency of an ordinary permanent magnet motor (OPM) is 92.33%, due to the addition of the stator can and rotor can, the efficiency of a permanent magnet caned motor (PMCM) is usually 86.58%. Loss results and efficiency comparisons are shown in Table 2.

The cam losses generate a lot of heat during operation. Therefore, the calculation method of cans losses considering the influence of temperature is proposed. The electromotive force under the fundamental magnetic field and harmonic magnetic field can be expressed as:

TABLE 3. Harmonic value of can losses.

Variable	Stator can(W)	Rotor can(W)
1	45.2048	0
3	0.3892	1.4114
5	0.0306	0.4435
7	0.0048	0.1583
9	0.0011	0.0642
11	3.49×10^{-4}	0.0317
13	1.46×10^{-4}	0.0191
15	6.86×10^{-5}	0.0122
17	1.04×10^{-4}	0.0242
19	7.51×10^{-6}	0.0022

$$\begin{cases} E_{m1} = B_{m1}\sin\left(\dfrac{\pi}{\tau}x\right) l_{\mathrm{ef}} V_{m1} = B_{m1}\sin\left(\dfrac{2p}{D}x\right) l_{\mathrm{ef}} V_{m1} \\ E_{xv} = B_v \sin\left(\dfrac{\pi}{\tau}x\right) l_{\mathrm{ef}} V_v = B_v \sin\left(\dfrac{2pv}{D}x\right) l_{\mathrm{ef}} V_v \end{cases} \tag{22}$$

Due to the uneven heat dissipation effect of the cooling channel, the conductivity of the cans will also change with the temperature, and the change law is as follows:

$$\sigma_{\mathrm{T}_1} = \frac{\sigma_{\mathrm{T}_0}}{\delta_{\mathrm{m}}\left[T_1 - T_0\right] + 1} \tag{23}$$

Combining the above two formulas, the following results can be obtained:

$$R_{\mathrm{m}} = \frac{l_{\mathrm{ef}}\left[\delta_{\mathrm{m}}\left(T_1 - T_0\right) + 1\right]}{\pi\sigma_{\mathrm{T}_0}\left(r_{\mathrm{m2}}^2 - r_{\mathrm{m1}}^2\right)} \tag{24}$$

Then the calculation formula of eddy current loss of cans can be expressed as:

$$\begin{aligned} p_{\mathrm{can}} &= p_{\mathrm{can1}} + p_{\mathrm{can}\upsilon} = \frac{E_{m1}^2}{R_{\mathrm{m1}}} + \sum_{\upsilon}\frac{E_{x\upsilon}^2}{R_{x\upsilon}} \\ &= \frac{B_{m1}^2 \sin^2\left(\frac{2p}{D}x\right) l_{\mathrm{ef}} V_{\mathrm{m1}}^2 \pi\sigma_{\mathrm{T}_0}\left(r_{\mathrm{m2}}^2 - r_{\mathrm{m1}}^2\right)}{\left[\delta_{\mathrm{m}}\left(T_1 - T_0\right) + 1\right]} \\ &\quad + \sum_{\upsilon}\frac{B_\upsilon^2 \sin^2\left(\frac{2pv}{D}x\right) l_{\mathrm{ef}} V_\upsilon^2 \pi\sigma_{\mathrm{T}_0}\left(r_{\mathrm{m2}}^2 - r_{\mathrm{m1}}^2\right)}{\left[\delta_{\mathrm{m}}\left(T_1 - T_0\right) + 1\right]} \end{aligned} \tag{25}$$

The magnetic density distribution at the center of the stator can(r = 24.1mm) and rotor can(r = 24.9mm) can be obtained according to equation (20).The results of the magnetic field in the section B are introduced into (25). The can losses of the PMCM can be obtained, and the results are shown in Table 3. The rotor can is attached to the outside of the rotor core and

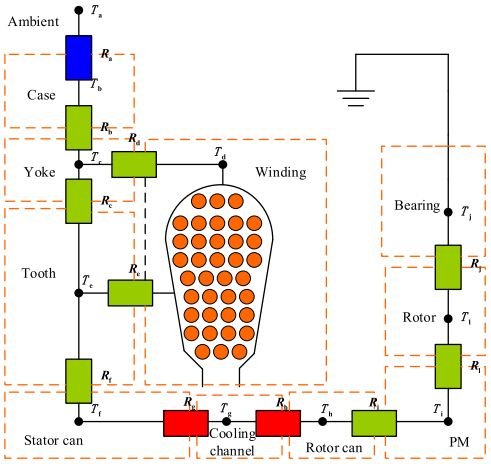

FIGURE 5. TNM of PMCM.

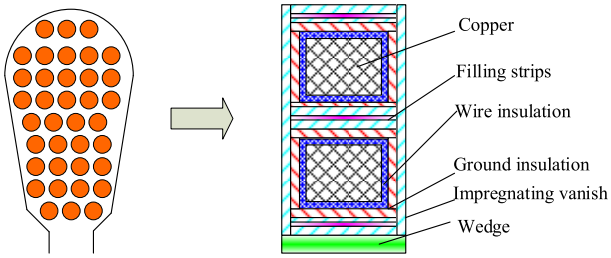

FIGURE 6. Equivalent model for thermal resistance of stator slots.

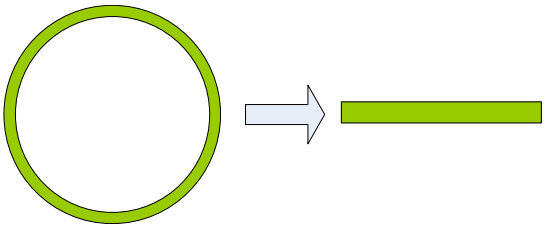

FIGURE 7. Cans equivalence.

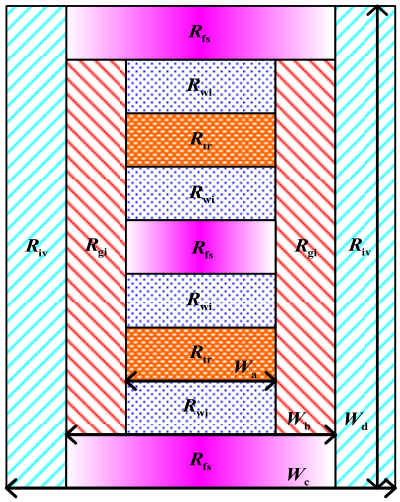

FIGURE 8. Thermal resistance model of stator slot.

rotates together with the rotor. The eddy current losses in the rotor can will be divided into those caused by the eddy currents induced by the fundamental and harmonic magnetic fields. As the fundamental magnetic field and the rotor rotate at synchronous speed, the relative speed is zero and does not cut the magnetic field. As a result, the eddy current losses in the rotor can caused by the fundamental magnetic field are 0W.

III. THERMAL NETWORK MODEL

The traditional heat network model is a fast and accurate calculation model, but this model considers that the heat flow in the object is constant. In fact, the conduction of heat flow in the body is linear, resulting in a certain deviation in the theoretical calculation of temperature rise. In considering the heat transfer phenomenon in the stator slot, the effects of material properties, geometry, boundary conditions, internal energy sources and other factors are considered. The equivalent stator slot model considers the effects of geometry through the equal area rule, the effects of material properties and boundary conditions through the heat dissipation coefficients of the different parts, and the effects of internal energy sources through whether each part is a source of heat generation. The same is obtained when solving for the heat dissipation coefficient of the cans. At the same time, without taking into account the uneven distribution of the can temperature, the heat dissipation coefficient of the solved TNM is a constant value, which is not the same as the actual situation, and the heat dissipation coefficient of the cans in this case is often chosen as the average value at room temperature, which results in a low can temperature. To solve the shortcomings of the traditional TNM, a TNM considering the uneven heat dissipation of the cooling channel is proposed in this paper, and the thermal resistance calculation formula is improved.

A. ESTABLISHMENT OF TNM

In addition to the winding model, the TNM is established using the simplified lumped parameter thermal network principle, as shown in Fig. 5. The calculation formulas of thermal resistance shown in Fig. 5 are given in the appendix and will not be mentioned in the article.

The model is based on the cylinder thermal resistance formula as follows:

$$R_{\mathrm{aa}} = \frac{L}{kA} = \frac{\ln(\frac{r_2}{r_1})}{k \cdot 2\pi l} \tag{26}$$

Equation (26) applies to cylindrical areas such as case, yokes, PM, and rotors. The thermal resistance between two components can be considered as half of each element. In Fig. 5, red thermal resistance indicates convection, green indicates conduction, and blue indicates natural convection. For simplicity, power and thermal capacity are hidden. The stationary solution can be obtained by

$$GT = P \tag{27}$$

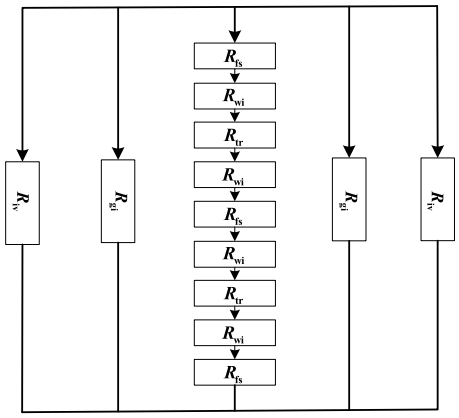

FIGURE 9. Simplified model of stator slot thermal resistance.

To facilitate the subsequent thermal network calculation, the winding and cans are simplified. The simplified model and simplified process are shown in Fig. 6 and Fig. 7. The derivation of winding thermal resistance will be given in the second subsection, and the derivation of cans thermal resistance will be provided in the third subsection.

B. WINDING THERMAL RESISTANCE

To better optimize the stator winding, the whole stator slot needs to be modeled, as shown in Fig. 8. To calculate the thermal resistance of each part of the winding more conveniently, it is necessary to simplify the winding model, which is shown in Fig. 9.

After simplifying the winding model, each thermal resistance shown in Fig. 9 is solved according to the principle of series-parallel connection of the circuit. The thermal resistance of wire insulation as follows:

$$R_{\mathrm{wi}} = \frac{(W_{\mathrm{b}} - W_{\mathrm{a}})/2}{W_{\mathrm{a}} \cdot d \cdot \lambda_{\mathrm{ep}}} \tag{28}$$

The thermal resistance of ground insulation as follows:

$$R_{\mathrm{gi}} = \frac{W_{\mathrm{d}} - 2 \cdot (W_{\mathrm{c}} - W_{\mathrm{b}})/2}{(W_{\mathrm{b}} - W_{\mathrm{a}})/2 \cdot d \cdot \lambda_{\mathrm{ep}}} \tag{29}$$

The thermal resistance of winding is as follows:

$$R_{\mathrm{tr}} = \frac{W_{\mathrm{a}}}{W_{\mathrm{a}} \cdot d \cdot \lambda_{\mathrm{cu}}} \tag{30}$$

The thermal resistance of filling strips is as follows:

$$R_{\mathrm{fs}} = \frac{(W_{\mathrm{c}} - W_{\mathrm{b}})/2}{W_{\mathrm{b}} \cdot d \cdot \lambda_{\mathrm{air}}} \tag{31}$$

The thermal resistance of impregnating vanish is as follows:

$$R_{\mathrm{iv}} = \frac{W_{\mathrm{c}}}{(W_{\mathrm{c}} - W_{\mathrm{b}})/2 \cdot d \cdot \lambda_{\mathrm{air}}} \tag{32}$$

The formula for solving the equivalent thermal resistance of winding is as follows:

$$R_{\mathrm{eq}} = \frac{d}{W_{\mathrm{c}} \cdot W_{\mathrm{d}} \cdot \lambda_{\mathrm{EQ}}} \tag{33}$$

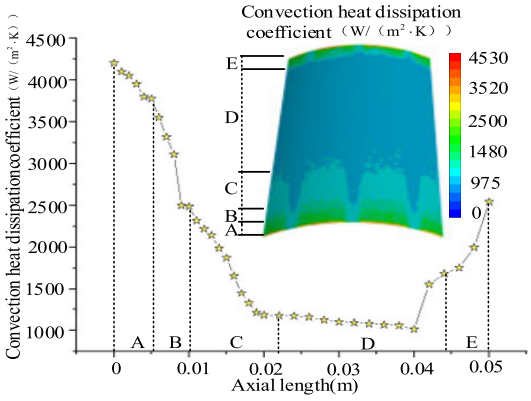

(a)

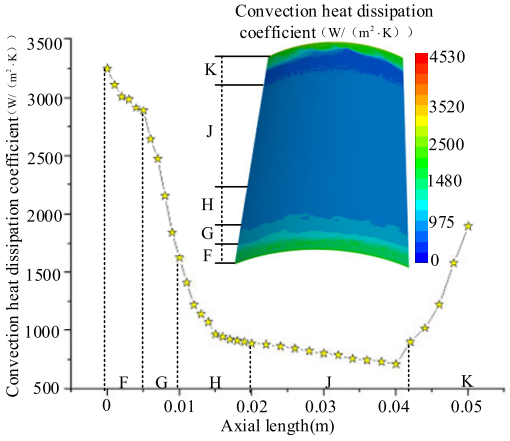

(b)

FIGURE 10. Convection heat dissipation coefficient: (a)stator can; (b) rotor can.

According to the circuit principle, the equivalent heat dissipation coefficient of the winding is obtained:

$$\frac{1}{R_{\mathrm{eq}}} = \frac{2}{R_{\mathrm{iv}}} + \frac{2}{R_{\mathrm{gi}}} + \frac{1}{4R_{\mathrm{wi}} + 2R_{\mathrm{tr}} + 3R_{\mathrm{fs}}} \tag{34}$$

$$\lambda_{\mathrm{EQ}} = \left(\frac{2}{R_{\mathrm{iv}}} + \frac{2}{R_{\mathrm{gi}}} + \frac{1}{4R_{\mathrm{wi}} + 2R_{\mathrm{tr}} + 3R_{\mathrm{fs}}}\right) \cdot d \Big/ W_{\mathrm{c}} \Big/ W_{\mathrm{d}} \tag{35}$$

Substituting the obtained heat dissipation coefficient into the thermal resistance calculation formula in the appendix can get the required thermal resistance results.

C. CAN THERMAL RESISTANCE

The heat dissipation resistance is closely related to the heat dissipation coefficient, and the heat dissipation performance of motor cooling fluid is related to its flow, velocity, and other factors. Therefore, the calculation accuracy of the thermal network largely depends on the accurate selection of convection heat dissipation coefficient on the fluid-solid interface. In this section, CFD technology will be used to establish the fluid domain of the cooling medium of this motor, and the

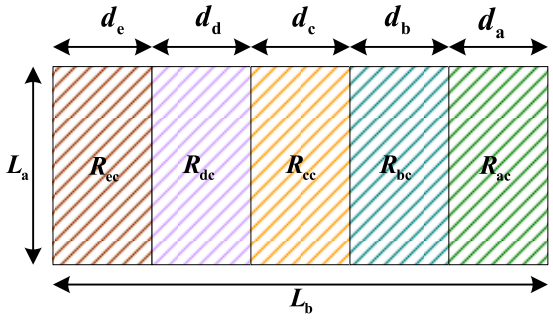

FIGURE 11. Stator can TNM.

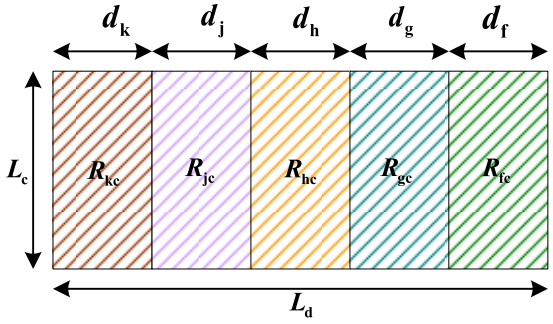

FIGURE 12. Rotor can TNM.

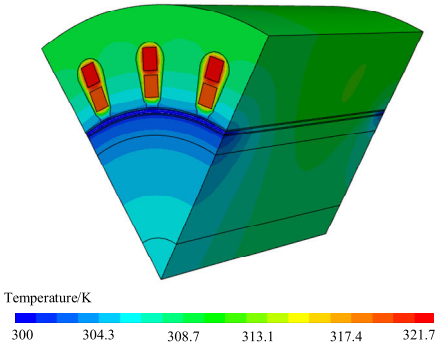

FIGURE 13. Temperature distribution.

interface heat dissipation coefficient will be directly obtained, or the convection heat dissipation coefficient will be determined by the empirical formula method according to the fluid flow rate.

The fluid field model of the motor is built into Fluent software. The convection heat dissipation coefficient of the cans of the PMCM is shown in Fig.10. As shown in Fig.10, the stator and rotor can are divided into five sections, each with different lengths. At an axial distance of 0.04m, the distance to the outlet is only 0.01m. Since the coolant enters from the inlet, its heat dissipation capacity is strongest at the inlet, hence the convective heat transfer coefficient is maximum at the inlet. As the coolant progresses, it absorbs more and more heat, resulting in a weakening of its heat dissipation capacity. At the outlet, 0.05m away, since there is no anti-backflow device in the cooling channel, there will be a reflux of coolant at the outlet, causing secondary heat dissipation at the outlet.

TABLE 4. Comparison of TNM and FEA results.

Symbol	Quantity	TNM(K)	FEA(K)
T_a	ambient temperature	300	300
T_b	case temperature	313.5	311.6
T_c	yoke temperature	317.2	312.7
T_d	winding temperature	322.2	321.7
T_e	tooth temperature	317.3	313.1
T_f	stator can temperature	320.9	314.7
T_g	cooling channel temperature	309.1	308.9
T_h	rotor can temperature	317.7	313.5
T_i	PM temperature	315.5	309.5
T_l	rotor temperature	313.1	308.6
T_j	bearing temperature	311.9	307.9

As a result, the convective heat transfer coefficient at the outlet is not the smallest, but rather the smallest at 0.04m.

It can be seen that the convection heat dissipation coefficient between the stator and rotor can, and the cooling fluid is not a constant value but changes continuously with the rotor rotation process. When the motor reaches the rated operating condition, it can be seen that the convection heat dissipation coefficient of the stator can be roughly divided into five sections according to the axial length. The division section of the convection heat dissipation coefficient of the rotor can is the same as that of the stator can.

The thermal network of the stator and rotor can is shown in Figs. 11 and 12. Thus, the heat dissipation coefficient of the stator can is obtained as follows:

$$\alpha_s = (\alpha_a d_a + \alpha_b d_b + \alpha_c d_c + \alpha_d d_d + \alpha_e d_e)/L_b \quad (36)$$

The analysis process of rotor can is similar to that of the stator can, which will not be repeated here. Similarly, the equivalent convection heat transfer coefficient of the rotor can be obtained as follows:

$$\alpha_{ss} = (\alpha_f d_f + \alpha_g d_g + \alpha_h d_h + \alpha_j d_j + \alpha_k d_k)/L_d \quad (37)$$

Substituting the obtained heat dissipation coefficient into the thermal resistance calculation formula in the appendix can get the required thermal resistance results.

IV. TEMPERATURE FIELD CALCULATION RESULTS AND FEA VERIFICATION

To verify the correctness of the results of thermal network calculation, a 750W PMCM is taken as the research object, and its temperature field model is established in fluent. Its temperature distribution is shown in Fig. 13.

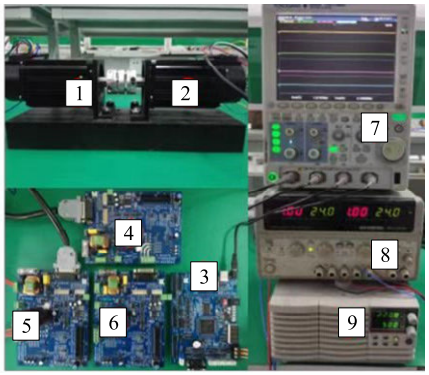

FIGURE 14. Experiment rig: 1-PMCM, 2-hysteresis dynamometer, 3, 4, 5, 6-Driver, 7-oscilloscope, 8, 9-DC source.

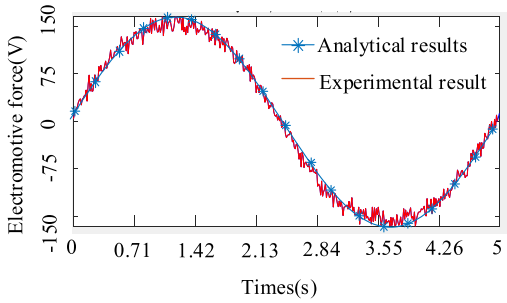

FIGURE 15. Comparison results.

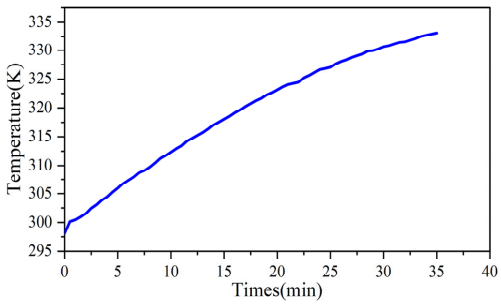

FIGURE 16. Temperature profile of the case over time.

TABLE 5. Comparison of TNM and experimental results.

Quantity	TNM(K)	Experiment(K)
Case temperature	330.96	332.95
Winding temperature	345.55	345.95

The radial temperature of the centerline is extracted from the results calculated by the FEA and compared with the results of the TNM, as shown in Table 4. The TNM proposed in this paper, mainly for the stator slot with the stator can and rotor can part of the local optimization, optimization of the part of the error is small, the stator part of the error is larger. And the power of this motor is 750W and its corresponding loss values are on the low side, which, together with the corresponding water-cooled cooling system, results in a maximum temperature rise of only 20K.

V. EXPERIMENTAL VERIFICATION

To validate the proposed method of subdomain method and can losses, experimental tests of electromotive force and temperature field are implemented on a platform. The experimental rig is shown in Fig. 14, and the main parameters of the tested prototype used in the experiments are listed in Table 1. The comparison results of the electromotive force are shown in Fig. 15. The comparison results of the temperature field are shown in Table 4. When doing temperature experiments for verification, as the prototype does not contain a water cooling system. Therefore, the temperature profile of the case measured in Fig. 16 will be higher than the temperatures discussed in this paper. Table 5 gives the results of the temperature comparison between the case and the winding. Where the case temperature is obtained from a thermistor connected to a temperature indicator and the winding temperature is estimated by the resistance method. The resistance method is based on the change in resistance as the coil heats up, to measure the coil temperature. The relationship between resistance and temperature satisfies the following equation:

$$T_{\text{hot}} = \frac{R_{\text{hot}}}{R_{\text{cold}}}(T_{\text{cold}} + 234.5) - 234.5 \tag{38}$$

It can be seen that the electromotive force calculated by the analytical method is consistent with the experimental measured electromotive force, which directly verifies the correctness of the subdomain method in this paper. In addition, it can be seen from Formula (22) that the induced electromotive force is required to calculate can losses. The comparison results indirectly verify the rationality of the computed results of the electromotive force in the can losses. Finally, the case and winding temperatures obtained from the TNM and the experimental method are compared in the temperature section. The two values are closer, further validating the correctness of the analytical model developed.

VI. CONCLUSION

To effectively improve the thermal analysis of PMCM, the magnetic field results obtained by the subdomain method are used to calculate the harmonic loss, and the heat dissipation coefficients of winding and cans in TNM are optimized by referring to the circuit principle. The following conclusions are obtained from the study.

The Laplace and Poisson equations in polar coordinates have been solved in the slot, air gap and PMs sub-domains by means of variable separation techniques. Solutions have been obtained using boundary and continuity conditions. The flux density is close to the FE prediction.

The can losses of PMCM are mainly based on the fundamental can losses of stator can. Therefore, it is impossible to reduce can losses through harmonic suppression technology. The reasonable design scheme can only be given through electromagnetic design.

The TNM can simulate the non-negligible temperature gradient in the groove and tooth areas, as well as the scene of uneven heat dissipation of the cans, even in the thermal stable

state. The calculation accuracy of other components will be significantly improved under the accurate winding and cans model.

The TNM is calculated with a lower calculation time, including winding temperature distribution, can temperature distribution, and steady-state temperature.

APPENDIX

In Fig.5, the PMCM is divided into eleven parts: environment, housing, yoke, teeth, winding, stator can, cooling channel, rotor can, PM, rotor and bearing.

On the basis of TNM, the main thermal conductivity between parts can be calculated with sufficient accuracy by analyzing the equation.

R_a- Conduction thermal resistance between case and ambient

$$R_a = \frac{1}{\pi \alpha_w \left[(D_s/2)^2 - (D_s/2 - h_{e1})^2\right]} \tag{A1}$$

$$\alpha_w = 14(1 + 0.5\sqrt{\omega})^3 \sqrt{\frac{T_0}{25}} \tag{A2}$$

where, ω is the wind speed outside the case,T_0 is the temperature outside the motor, D_s is the diameter of the stator, h_{e1} is the height of the stator yoke.

R_b-Conduction thermal resistance between case and yoke

$$R_b = \frac{1}{2\pi\lambda_{tie}L/3} \ln\left(\frac{D_{s1}/2}{D_{s1}/2 - h_{e1}/2}\right) + \frac{1}{2\pi\lambda_{qi}L/3} \ln\left(\frac{D_{s1}/2 + L_b}{D_{s1}/2}\right) + \frac{1}{2\pi\lambda_{ke}L/3} \ln\left(\frac{D_{ke}/2 - h_{yke}/2}{D_{s1}/2 + L_b}\right) \tag{A3}$$

where, $\lambda_{tie/qi/ke}$ is the thermal conductivity of the stator, air and casing, D_{s1} is the outer diameter of the stator, h_{yke} is the thickness of the casing, D_{ke} is the height of the case, L is axial length of stator.

The gap between the case and the stator core can be obtained from the empirical formula:

$$L_b = (0.5 + 3D_s) \times 10^{-5} \tag{A4}$$

R_c- Conduction thermal resistance between tooth and yoke

$$R_c = \frac{(D_{s1} - D_{s2})/4}{\lambda_{tie} Z_a b_c L/3} \tag{A5}$$

where, b_c is the yoke width of the stator, D_{s2} is the inner diameter of the stator and Z_a is number of stator slots.

R_d- Conduction thermal resistance between winding and yoke

$$R_d = \frac{h_{e1}/2}{\lambda_{tie} S_d} + \frac{h_{coil}/2}{\lambda_{EQ} S_d} \tag{A6}$$

$$S_d = \frac{\pi R_{ar} Z_a L}{3} \tag{A7}$$

where, h_{coil} is the height of stator winding, R_{ar} is the arc radius of slot bottom.

R_e- Conduction thermal resistance between winding and tooth

$$R_e = \frac{b_{coil}/2}{\lambda_{EQ} S_e} + \frac{b_a}{\lambda_{tie} S_e} \tag{A8}$$

$$S_e = \frac{2Z_a h_s L}{3} \tag{A9}$$

where, h_s is the height of the stator slot, b_a is the tooth width of the stator and b_{coil} is the equivalent width of the copper winding in the stator slot.

R_f- Conduction thermal resistance between tooth and stator can

$$R_f = \frac{L_s/3}{\lambda_{tie} b_a L_s Z_a} \tag{A10}$$

where, L_s is axial length of stator can.

R_g- Conduction thermal resistance between water and stator can

$$R_g = \frac{1}{\alpha_s \pi \left(R_{w1}^2 - R_{w2}^2\right)} \tag{A11}$$

where, R_{w1}andR_{w2} is the outer and inner radius of stator can.

R_h- Conduction thermal resistance between water and rotor can

$$R_h = \frac{1}{\alpha_{ss} \pi \left(R_{w3}^2 - R_{w4}^2\right)} \tag{A12}$$

where, $R_{w3}$and R_{w4} is the outer and inner radius of rotor can.

R_i- Conduction thermal resistance between PM and rotor can

$$R_i = \frac{(D_{02} - D_{01})/3}{\lambda_{pm} S_i} \tag{A13}$$

$$S_i = \pi D_{02} L_i \tag{A14}$$

where, $D_{01}$and D_{02} is the inner and outer diameter of the permanent magnet, λ_{pm} is the thermal conductivity of PM and L_i is axial length of PM.

R_l- Conduction thermal resistance between PM and rotor

$$R_l = \frac{(D_{02} - D_{01})/4}{\lambda_{pm} S_l} \tag{A15}$$

$$S_l = \pi D_{01} L_i \tag{A16}$$

R_j- Conduction thermal resistance between bearing and rotor

$$R_j = \frac{L_j + L_i/6}{\lambda_{tie} S_j} \tag{A17}$$

$$S_j = \pi D_{03} L_j \tag{A18}$$

where, D_{03} is the inner diameter of the rotor and L_j is axial length of rotor.

REFERENCES

[1] L. Gao, J. Wei, C. Li, and Y. Liang, "Analyses on performances of megawatt double-canned induction motors with different can materials," *IEEE Trans. Energy Convers.*, vol. 32, no. 2, pp. 667–674, Jun. 2017.

[2] Y. Liang, L. Gao, C. Li, and Y. Hu, "Investigation of end leakage reactance and its influence on the accuracy in performance calculation of large double canned induction motors," *IEEE Trans. Ind. Electron.*, vol. 65, no. 2, pp. 1420–1428, Feb. 2018.

[3] D. Uneyama, Y. Akiyama, S. Manome, and T. Naruta, "The proposal of can loss estimation method of canned motor," in *Proc. Int. Conf. Electr. Mach. Syst. (ICEMS)*, Oct. 2007, pp. 882–885.
[4] Q. Yu, X. Wang, and Y. Cheng, "Electromagnetic calculation and characteristic analysis of can effect of a canned permanent magnet motor," *IEEE Trans. Magn.*, vol. 52, no. 12, pp. 1–6, Dec. 2016.
[5] Q. Yu, S. Chu, W. Li, L. Tian, X. Wang, and Y. Cheng, "Electromagnetic shielding analysis of a canned permanent magnet motor," *IEEE Trans. Ind. Electron.*, vol. 67, no. 10, pp. 8123–8130, Oct. 2020.
[6] H. Tang, J. Di, Z. Wu, and W. Li, "Temperature analysis for the asymmetric six-phase permanent magnet synchronous motor in healthy and fault-tolerant modes," *IEEE Trans. Ind. Electron.*, vol. 70, no. 7, pp. 6482–6493, Jul. 2023.
[7] L. J. Wu, Z. Q. Zhu, D. Staton, M. Popescu, and D. Hawkins, "Subdomain model for predicting armature reaction field of surface-mounted permanent-magnet machines accounting for tooth-tips," *IEEE Trans. Magn.*, vol. 47, no. 4, pp. 812–822, Apr. 2011.
[8] T. Lubin, S. Mezani, and A. Rezzoug, "2-D exact analytical model for surface-mounted permanent-magnet motors with semi-closed slots," *IEEE Trans. Magn.*, vol. 47, no. 2, pp. 479–492, Feb. 2011.
[9] C. Chen, X. Wu, X. Yuan, and X. Zheng, "A new technique for the subdomain method in predicting electromagnetic performance of surface-mounted permanent magnet motors with shaped magnets and a quasi-regular polygon rotor core," *IEEE Trans. Energy Convers.*, vol. 38, no. 2, pp. 1396–1409, Jun. 2023.
[10] W. Tong, S. Li, X. Pan, S. Wu, and R. Tang, "Analytical model for cogging torque calculation in surface-mounted permanent magnet motors with rotor eccentricity and magnet defects," *IEEE Trans. Energy Convers.*, vol. 35, no. 4, pp. 2191–2200, Dec. 2020.
[11] S. T. Boroujeni, S. P. Emami, and P. Jalali, "Analytical modeling of eccentric PM-inset machines with a slotless armature," *IEEE Trans. Energy Convers.*, vol. 34, no. 3, pp. 1466–1474, Sep. 2019.
[12] L. Wu, H. Yin, D. Wang, and Y. Fang, "On-load field prediction in SPM machines by a subdomain and magnetic circuit hybrid model," *IEEE Trans. Ind. Electron.*, vol. 67, no. 9, pp. 7190–7201, Sep. 2020.
[13] Y. Zhou, H. Li, N. Ren, Z. Xue, and Y. Wei, "Analytical calculation and optimization of magnetic field in spoke-type permanent-magnet machines accounting for eccentric pole-arc shape," *IEEE Trans. Magn.*, vol. 53, no. 9, pp. 1–7, Sep. 2017.
[14] Y. Zhou, H. Li, G. Meng, S. Zhou, and Q. Cao, "Analytical calculation of magnetic field and cogging torque in surface-mounted permanent-magnet machines accounting for any eccentric rotor shape," *IEEE Trans. Ind. Electron.*, vol. 62, no. 6, pp. 3438–3447, Jun. 2015.
[15] L. Jing, W. Liu, W. Tang, and R. Qu, "Design and optimization of coaxial magnetic gear with double-layer PMs and spoke structure for tidal power generation," *IEEE/ASME Trans. Mechatronics*, early access, Apr. 11, 2023, doi: 10.1109/TMECH.2023.3261987.
[16] L. Jing, W. Tang, T. Wang, T. Ben, and R. Qu, "Performance analysis of magnetically geared permanent magnet brushless motor for hybrid electric vehicles," *IEEE Trans. Transport. Electrific.*, vol. 8, no. 2, pp. 2874–2883, Jun. 2022.
[17] L. Fang, D. Li, and R. Qu, "Torque improvement of Vernier permanent magnet machine with larger rotor pole pairs than stator teeth number," *IEEE Trans. Ind. Electron.*, vol. 70, no. 12, pp. 12648–12659, Dec. 2023.
[18] A. Boglietti, M. Cossale, M. Popescu, and D. A. Staton, "Electrical machines thermal model: Advanced calibration techniques," *IEEE Trans. Ind. Appl.*, vol. 55, no. 3, pp. 2620–2628, May 2019.
[19] S. Zhu, M. Cheng, and X. Cai, "Direct coupling method for coupled field-circuit thermal model of electrical machines," *IEEE Trans. Energy Convers.*, vol. 33, no. 2, pp. 473–482, Jun. 2018.
[20] O. Wallscheid and J. Böcker, "Global identification of a low-order lumped-parameter thermal network for permanent magnet synchronous motors," *IEEE Trans. Energy Convers.*, vol. 31, no. 1, pp. 354–365, Mar. 2016.
[21] F. Ahmed and N. C. Kar, "Analysis of end-winding thermal effects in a totally enclosed fan-cooled induction motor with a die cast copper rotor," *IEEE Trans. Ind. Appl.*, vol. 53, no. 3, pp. 3098–3109, May 2017.
[22] X. Cai, M. Cheng, S. Zhu, and J. Zhang, "Thermal modeling of flux-switching permanent-magnet machines considering anisotropic conductivity and thermal contact resistance," *IEEE Trans. Ind. Electron.*, vol. 63, no. 6, pp. 3355–3365, Jun. 2016.
[23] L. Mo, X. Zhu, T. Zhang, L. Quan, Y. Wang, and J. Huang, "Temperature rise calculation of a flux-switching permanent-magnet double-rotor machine using electromagnetic-thermal coupling analysis," *IEEE Trans. Magn.*, vol. 54, no. 3, pp. 1–4, Mar. 2018.
[24] C. Sciascera, P. Giangrande, L. Papini, C. Gerada, and M. Galea, "Analytical thermal model for fast stator winding temperature prediction," *IEEE Trans. Ind. Electron.*, vol. 64, no. 8, pp. 6116–6126, Aug. 2017.
[25] X. Jiang, Y. Zhang, S. Jin, F. Zhang, and C. Gerada, "A novel thermal network model used for temperature calculation and analysis on brushless doubly-fed generator with winding encapsulating structure," *IEEE Trans. Ind. Appl.*, vol. 55, no. 2, pp. 1473–1483, Mar. 2019.
[26] A. J. Grobler, S. R. Holm, and G. van Schoor, "Empirical parameter identification for a hybrid thermal model of a high-speed permanent magnet synchronous machine," *IEEE Trans. Ind. Electron.*, vol. 65, no. 2, pp. 1616–1625, Feb. 2018.
[27] A. Boglietti, E. Carpaneto, M. Cossale, and S. Vaschetto, "Stator-winding thermal models for short-time thermal transients: Definition and validation," *IEEE Trans. Ind. Electron.*, vol. 63, no. 5, pp. 2713–2721, May 2016.
[28] D. Wang, D. Zhang, X. Du, and X. Wang, "Thermal identification, model, and experimental validation of a toroidally wound mover linear-switched reluctance machine," *IEEE Trans. Magn.*, vol. 54, no. 3, pp. 1–5, Mar. 2018.
[29] N. Simpson, R. Wrobel, and P. H. Mellor, "Estimation of equivalent thermal parameters of impregnated electrical windings," *IEEE Trans. Ind. Appl.*, vol. 49, no. 6, pp. 2505–2515, Nov. 2013.
[30] P. Taras, G.-J. Li, Z.-Q. Zhu, M. P. Foster, and D. A. Stone, "Combined multiphysics model of switched flux PM machines under fault operations," *IEEE Trans. Ind. Electron.*, vol. 66, no. 9, pp. 6737–6745, Sep. 2019.
[31] X. Fan, R. Qu, J. Li, D. Li, B. Zhang, and C. Wang, "Ventilation and thermal improvement of radial forced air-cooled FSCW permanent magnet synchronous wind generators," *IEEE Trans. Ind. Appl.*, vol. 53, no. 4, pp. 3447–3456, Jul. 2017.
[32] Z. Zhang, Y. Wang, Y. Sang, and L. Yu, "Efficiency improvement and thermal analysis of a totally enclosed self-cooling doubly salient generator with optimized stator yoke," *IEEE Trans. Magn.*, vol. 52, no. 7, pp. 1–5, Jul. 2016.

LIANLIAN GAO was born in 1990. She received the Ph.D. degree in electrical machine from the Harbin University of Science and Technology, Harbin, China, in 2018.

She is currently a Lecturer with the Harbin University of Science and Technology. Her current research interests include energy conversion mechanisms, analysis and numerical calculation of comprehensive physical fields, motor electromagnetic theory, and new technology.

HUI LIU was born in Shanxi, China, in 1998. He is currently pursuing the M.S. degree in electrical machines with the Harbin University of Science and Technology, Harbin, China. His current research interests include permanent magnet motor electromagnetic theory and design and electromagnetic field calculation.

QUN NIU was born in 1997. He received the bachelor's degree from the Harbin University of Science and Technology, Harbin, China, in 2019, where he is currently pursuing the Graduate degree. His current research interest includes the analysis and numerical calculation of comprehensive physical field.